

Spin-Flip Raman Scattering on Electrons and Holes in Two-Dimensional (PEA)₂PbI₄ Perovskites

C. Harkort,¹ D. Kudlacik,¹ N. E. Kopteva,¹ D. R. Yakovlev,¹ M. Karzel,¹

E. Kirstein,¹ O. Hordiichuk,^{2,3} M. Kovalenko,^{2,3} and M. Bayer¹

¹*Experimentelle Physik 2, Technische Universität Dortmund, D-44221 Dortmund, Germany*

²*Laboratory of Inorganic Chemistry, Department of Chemistry and Applied Biosciences, ETH Zürich, CH-8093 Zürich, Switzerland and*

³*Laboratory for Thin Films and Photovoltaics, Empa-Swiss Federal Laboratories for Materials Science and Technology, CH-8600 Dübendorf, Switzerland*

(Dated: February 7, 2023)

The class of Ruddlesden-Popper type (PEA)₂PbI₄ perovskites comprises two-dimensional (2D) structures whose optical properties are determined by excitons with a large binding energy of about 260 meV. It complements the family of other 2D semiconductor materials by having the band structure typical for lead halide perovskites, that can be considered as inverted compared to conventional III-V and II-VI semiconductors. Accordingly, novel spin phenomena can be expected for them. Spin-flip Raman scattering is used here to measure the Zeeman splitting of electrons and holes in a magnetic field up to 10 T. From the recorded data, the electron and hole Landé factors (g -factors) are evaluated, their signs are determined, and their anisotropies are measured. The electron g -factor value changes from +2.11 out-of-plane to +2.50 in-plane, while the hole g -factor ranges between -0.13 and -0.51 . The spin flips of the resident carriers are arranged via their interaction with photogenerated excitons. Also the double spin-flip process, where a resident electron and a resident hole interact with the same exciton, is observed showing a cumulative Raman shift. Dynamic nuclear spin polarization induced by spin-polarized holes is detected in corresponding changes of the hole Zeeman splitting. An Overhauser field of the polarized nuclei acting on the holes as large as 0.6 T can be achieved.

I. INTRODUCTION

Lead halide perovskite semiconductors attract nowadays great attention due to their remarkable potential for photonic applications [1–4]. They are available as bulk- and nanocrystals and also as two-dimensional (2D) layered materials. 2D perovskites feature exceptional optical and electrical properties. By changing the thickness of the semiconductor layers and varying the organic barriers, their band gap energy changes from the infrared up to the ultraviolet spectral range [5–7]. The 2D perovskites exhibit robust environmental stability [8], which makes them promising for optoelectronic [4, 8, 9] and photovoltaic [10–12] applications. The strong quantum confinement of electrons and holes results in excitons with large binding energies, which are additionally increased by dielectric confinement, approaching 200–500 meV [13, 14]. The optical properties of 2D perovskites are therefore determined by exciton absorption and emission even in ambient conditions [15, 16], similar to 2D semiconductors like transition metal dichalcogenides [17].

The band gap in lead halide perovskites is located at the R-point of the Brillouin zone for cubic crystal lattice and at the Γ -point for tetragonal or orthorhombic lattices [18, 19]. In all these cases, the states at the bottom of the conduction band and the top of the valence band have spin 1/2. The perovskites band structure is inverted compared to conventional III-V and II-VI semiconductors, i.e., in the vicinity of the band gap the valence band is mostly formed by the s-orbitals of Pb, while the

conduction band states are contributed by the p-orbitals of Pb. As a result, the spin-orbit interaction modifies mostly the valence band states (and thus the hole effective mass and g -factor) [20–22], and the hyperfine interaction with the nuclear spins is much stronger for the holes than for the electrons, in contrast to conventional semiconductors [21]. Therefore, lead halide perovskites of different dimensionalities are considered as novel model systems for spin physics, offering interesting perspectives for spintronic and quantum information applications [23].

Recent studies show that a similar level of optical spin control can be achieved in perovskites as in conventional semiconductors. To that end, the optical and magneto-optical techniques established for studying spin-dependent phenomena were tested with respect to their suitability for lead halide perovskites: optical orientation [24–27], optical alignment [25], polarized emission in magnetic field [28–30], time-resolved Faraday/Kerr rotation [21, 31, 32] and spin-flip Raman scattering [22, 33] were demonstrated. Some of them were also used to study spin properties including their dynamics in 2D perovskites. Application of high magnetic fields up to 60 T provided information on the exciton fine structure and exciton Landé factor (g -factor) [34–41]. The exciton spin dynamics down to subpicosecond time scales were addressed by optical spin orientation measured by time-resolved transmission [42–46]. Most of the dynamical studies were carried out above liquid nitrogen up to room temperature, where the spin relaxation times do not exceed a few picoseconds. Recently, time-resolved Kerr rotation allowed measurements of the coherent dynamics of electron spins in the (PEA)₂PbI₄ 2D perovskite [47].

In these experiments, longitudinal spin relaxation times up to 25 μs were found at the temperature of 1.6 K. In addition, the electron g -factor was measured, showing a considerable anisotropy. At present, the experimental information on the electron and hole g -factors in 2D perovskites, being the key parameters for understanding and interpreting spin-dependent phenomena, is still limited, and we are also not aware of corresponding theoretical considerations.

Spin-flip Raman scattering (SFRS) spectroscopy is another powerful magneto-optical technique in spin physics, providing direct information on the Zeeman splitting of electrons, holes, and excitons, and on the optical selection rules due to the spin level structure of exciton complexes, determined by their symmetries and exciton-carrier spin interactions [48–54]. SFRS signals are strongly enhanced when the laser photon energy is tuned into resonance with the exciton. SFRS measurements are experimentally challenging due to the close spectral proximity of the spin-flip signals and the laser line, as the spin-flip Raman shift is on the order of a few hundred μeV . Recently, however, the feasibility of SFRS for measuring the electron and hole g -factors in CsPbBr_3 and MAPbI_3 lead halide perovskite crystals was demonstrated [22].

In this paper, we report on an SFRS study of the electron and hole g -factors in Ruddlesden-Popper type $(\text{PEA})_2\text{PbI}_4$ two-dimensional perovskites. The experiments are performed at cryogenic temperatures in magnetic fields up to 10 T, applied in different geometries in order to measure the g -factor anisotropy. The spin-flip signals originate from resident electrons and holes interacting with photogenerated excitons. Further, nuclear spin polarization by spin polarized holes is evidenced through corresponding shifts of the hole spin-flip line.

II. EXPERIMENTAL RESULTS

A. Optical properties of two-dimensional perovskites $(\text{PEA})_2\text{PbI}_4$

We study the 2D Ruddlesden-Popper type perovskite structure $(\text{PEA})_2\text{PbI}_4$, which consists of a corner-shared network of PbI_6 -octahedral monolayers constituting quantum wells separated by van der Waals-bonded pairs of PEA [phenethylammonium] molecules. Due to the strong quantum confinement of electrons and holes in the 2D perovskite layers, the band gap energy increases to 2.608 eV at $T = 2$ K [37]. The reduced dimensionality and the dielectric confinement effect [19], provided by the difference of dielectric constants between the perovskite and the PEA, strongly increase the exciton binding energy in $(\text{PEA})_2\text{PbI}_4$ to 260 meV [37, 41], in comparison to 16 meV in bulk MAPbI_3 [55].

The pronounced exciton resonance in $(\text{PEA})_2\text{PbI}_4$ is seen in the reflectivity (R) spectrum, measured at the temperature of $T = 1.6$ K, see Figure 1a. The resonance line with the minimum at 2.341 meV and the full width

at half maximum of 6.6 meV originates from the free exciton. In external magnetic field applied in the Faraday geometry ($\mathbf{B}_F \parallel \mathbf{k} \parallel c$), the exciton spin states $+1$ and -1 detected in σ^+ and σ^- circular polarization, respectively, are subject to Zeeman splitting by $E_{Z,X} = g_{X,c}\mu_B B_F$. Here, the c -axis is perpendicular to the 2D planes, \mathbf{k} is the light wave vector, $g_{X,c}$ is the exciton g -factor along the c -axis, and μ_B is the Bohr magneton. Reflectivity spectra at $B_F = 7$ T measured in σ^+ and σ^- polarization are shown in Figure 1b. The different energies of the exciton resonance in the two spectra reflect the Zeeman splitting. In Figure 1c we present the magnetic field dependence of the exciton Zeeman splitting, from its linear fit the exciton g -factor $g_{X,c} = +1.6 \pm 0.1$ is evaluated. Note that in this experiment the g -factor sign can be determined: a positive value corresponds to a high energy shift of the σ^+ polarized resonance relative to the σ^- polarized one.

The photoluminescence (PL) spectrum shows a strong emission line with the maximum at 2.343 eV and the full width at half maximum of about 10 meV, see Figure 1a. The PL line coincides in energy with the free exciton resonance measured in reflectivity. However, note that the PL line is broader than the reflectivity line. It is plausible to assign the line to the exciton emission of both free and weakly localized excitons. This assignment is supported by time-integrated and time-resolved spectroscopic studies at cryogenic temperatures reported in Refs. 38, 39, 56–58, showing that the PL band is composed of at least two emission lines. Their recombination dynamics show times in the range of 300 ps to 10 ns, highlighting the free- and bound-exciton origin.

For the studied $(\text{PEA})_2\text{PbI}_4$, the population dynamics are measured by time-resolved differential reflectivity for resonant excitation of the exciton. The results are reported in Ref. 47. The dynamics trace reveals decays with times of 20 ps and 340 ps. Also a longer-lived component with a decay exceeding 1 ns is observed. We attribute the short dynamics of 20 ps to the lifetime of the bright excitons with a large oscillator strength in 2D perovskites. The lifetime is given by their radiative recombination and their relaxation into dark exciton states. This interpretation is in agreement with literature data on the low temperature recombination dynamics in $(\text{PEA})_2\text{PbI}_4$ [57–59]. The slower 340 ps dynamics can be attributed to non-geminate recombination of charge carriers.

In Figure 1d, the PL dynamics measured at the maximum of the PL line across a much longer temporal range up to 100 μs are shown. Recombination processes with a decay time of about 40 μs are observed, which greatly exceeds the typical times in exciton dynamics. This evidences that long-living resident carriers are present in the studied structures. These resident carriers can be photo-generated electrons and holes which are localized at spatially separated sites. We will term them as resident electrons and holes and will show that they give the main contribution to the measured SFRS signals. Note that the existence of resident carriers is typical for lead

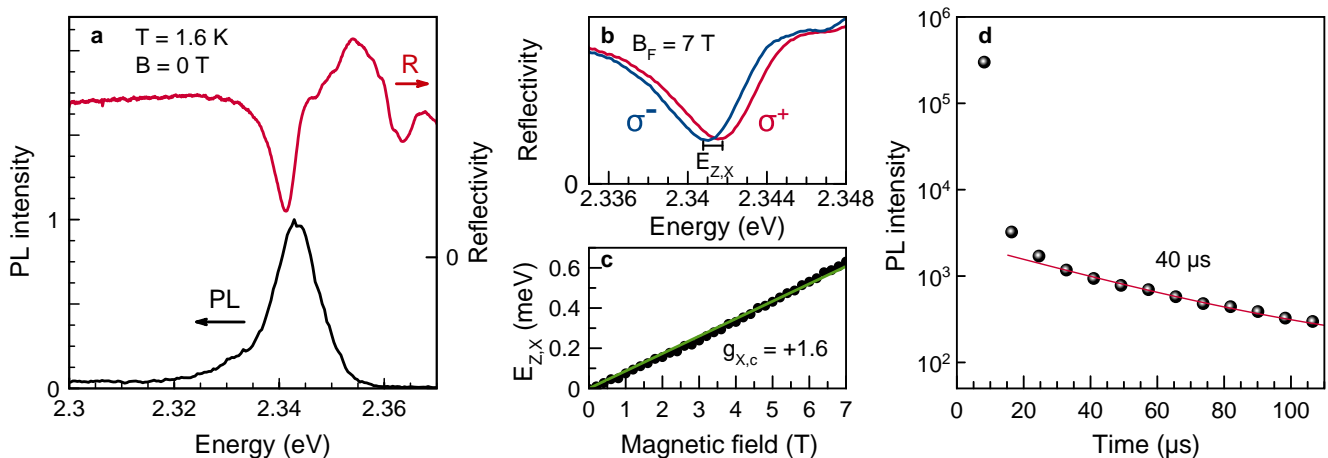


FIG. 1. Optical properties of excitons in (PEA)₂PbI₄ at $T = 1.6$ K. (a) Reflectivity (red) and photoluminescence (black) spectra. The PL is excited at 2.412 eV photon energy using $P = 10.8$ W/cm² excitation power. (b) Counter-circularly polarized reflectivity spectra measured in Faraday geometry at $B_F = 7$ T ($\mathbf{B}_F \parallel \mathbf{k} \parallel c$). The exciton Zeeman splitting of $E_{Z,x} = 0.63$ meV can be determined with good accuracy. (c) Magnetic field dependence of the exciton Zeeman splitting evaluated from magneto-reflectivity data (symbols). The green line is a B -linear fit. (d) PL dynamics (symbols) measured at the PL maximum of 2.343 eV. Pulsed excitation is used at an energy of 3.493 eV photon energy with an average power of $P = 3$ W/cm². The line is an exponential fit of the decay at longer time with the time constant of 40 μ s.

halide perovskites, as we showed for bulk CsPbBr₃ [32], FA_{0.9}Cs_{0.1}PbI_{2.8}Br_{0.2} [21], and MAPbI₃ [60] crystals using optical techniques.

The weak low energy flank of the PL line at 2.330 eV, see Figure 1a, was assigned in literature either to dark exciton emission [38, 56, 61] or to phonon-assisted bright exciton recombination [57].

B. Spin-flip Raman scattering in close-to-Faraday geometry

We apply spin-flip Raman scattering to study the properties of the resident carrier spins in the 2D (PEA)₂PbI₄ perovskite. In an external magnetic field, \mathbf{B} , the spin sublevels of the electrons (e) and the holes (h) are split by the Zeeman energy $E_{Z,e(h)} = g_{e(h)}\mu_B B$, which is proportional to the magnetic field strength and the electron (hole) g -factor $g_{e(h)}$. In the process of Raman light scattering, the carrier spin can flip changing its orientation, which requires either absorption or dissipation of the energy amount equal to $E_{Z,e(h)}$, depending on whether the spin flips from the lower to the upper energy level or vice versa. Therefore, the energy of the scattered photon differs from the laser photon energy by $E_{Z,e(h)}$. In case of energy absorption, the Raman shift occurs to lower energies (Stokes shift), note, however, that in SFRS experiments it is common to refer to this case as positive Raman shift. In case of energy dissipation, the shift is to larger energies (anti-Stokes shift), so that the Raman shift values are negative. For light scattering in semiconductors, an exciton serves as a mediator between light and spins [51, 52], because the light-matter interaction is

greatly enhanced at the exciton resonance.

The schematics of the applied experimental geometries are shown in Figure 2a. In the Faraday geometry the magnetic field is parallel to the light k -vector ($\mathbf{B}_F \parallel \mathbf{k}$), which in turn is parallel to the crystal c -axis ($\mathbf{k} \parallel c$). In the studied (PEA)₂PbI₄, SFRS signal is absent in the pure Faraday geometry, because the carrier spin states $+1/2$ and $-1/2$ are not mixed by magnetic field and, thus, the spin-flip process is suppressed. Such mixing already occurs for small tilt angles, e.g. at $\theta = 10^\circ$, and then indeed SFRS signals become pronounced. We refer to this geometry as "close-to-Faraday geometry", where the Zeeman splitting is dominated by the g -factor component along the c -axis ($g_{e(h),c}$). The SFRS spectrum measured at $B = 9.4$ T with the excitation laser tuned to the exciton resonance at 2.345 eV, is shown in Figure 2b. The spin-flip lines are more pronounced in the anti-Stokes spectral range, as there the contribution of background photoluminescence is minimized.

Four spin-flip lines in the SFRS spectrum labeled by E_h , E_{e+h} , E_e , and E_{e-h} are seen in Figure 2b. They are absent at zero magnetic field, as expected from the vanishing Zeeman splitting so that the spin-flip lines coincide with the exciting laser energy. With increasing magnetic field the lines shift linearly from the laser energy (referred to as zero). The details of their shifts are shown in Figures 3a,b,c. The E_h line is only detected in high magnetic fields (see the black circles in Figure 3c) due to its small shift amounting to only -0.078 meV at 9.4 T, which is associated with the spin-flip of the hole having $|g_{h,c}| = 0.13$. The electron spin-flip line shows a much larger shift of $E_e = -1.137$ meV at $B = 9.4$ T. Its magnetic field dependence in Figure 3a allows us to eval-

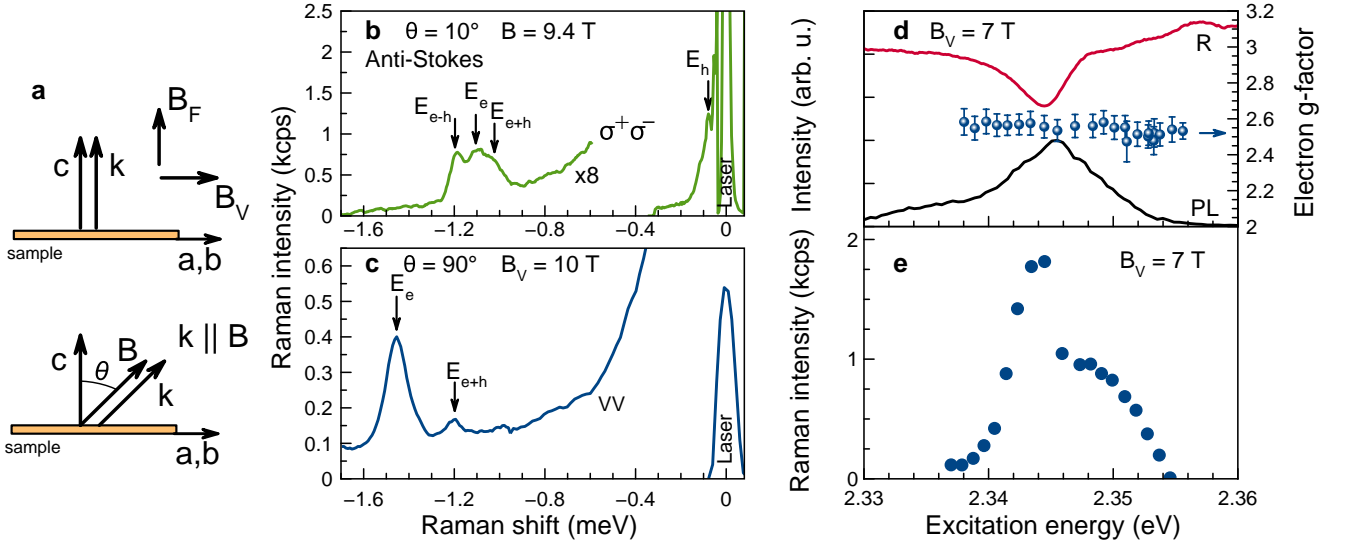


FIG. 2. Spin-flip Raman scattering in $(\text{PEA})_2\text{PbI}_4$. (a) Sketch of the experimental geometry. Upper diagram is for the Faraday ($\mathbf{B}_F \parallel c$) and Voigt ($\mathbf{B}_V \parallel (a, b)$) geometry with the laser light vector $\mathbf{k} \parallel c$. Bottom diagram is for the tilted field geometry. The angle θ specifies the tilt between \mathbf{B} and the c -axis ($\mathbf{k} \parallel \mathbf{B}$). (b) SFRS spectrum in the anti-Stokes spectral range (negative Raman shift) for $\theta = 10^\circ$, measured for $E_{\text{exc}} = 2.345$ eV laser photon energy with the power $P = 5.7$ W/cm 2 . The spectrum is multiplied by a factor of 8. The shifts of the hole E_h , the electron E_e , and their double flip (E_{e+h} and E_{e-h}) lines are marked with arrows. (c) SFRS spectrum in Voigt geometry at $B_V = 10$ T using linearly co-polarized excitation and detection. (d) Reflectivity and photoluminescence spectra at $B_V = 7$ T. Electron g -factor dependence on the excitation energy (circles). (e) SFRS intensity resonance profile for the electron spin-flip at $B_V = 7$ T. All data are measured at $T = 1.6$ K.

uate $|g_{e,c}| = 2.11$, agreeing well with $g_{e,c} = +2.05 \pm 0.05$ determined from time-resolved Kerr rotation on the same sample [47].

Identification of the hole and electron SFRS lines is done by comparing their g -factors with the universal dependence of the carrier g -factors on the band gap energy, that has recently been established for bulk lead halide perovskites [22]. According to this dependence for materials with band gap energies around 2.3 eV, g -factor values of $g_e \approx +2.0$ and $g_h \approx +0.7$ are predicted. We expect some, but not drastic deviations from this dependence for the 2D perovskites. Therefore, we assign the spin-flip line with the larger shift to the resident electron with positive sign of the g -factor.

Another approach to distinguish electrons from holes is based on their interactions with the nuclear spin system, since in lead halide perovskites the hole-nuclei interaction is about five times stronger than the electron-nuclei one [21]. This also leads to a much stronger dynamic nuclear polarization (DNP) by the holes. In Section II F we show that DNP can be detected with the SFRS technique and that its effect is considerable for the E_h line. Note that it is absent for the E_e line, in accordance with our assignment. From this experiment, the sign of the hole g -factor can be unambiguously determined. For the studied $(\text{PEA})_2\text{PbI}_4$, the hole g -factor is negative, i.e. $g_{h,c} = -0.13$.

The electron line E_e has two satellites, E_{e-h} and E_{e+h} , which are shifted by the hole Zeeman splitting. The

slopes in their magnetic field dependence give $|g_{e-h,c}| = 2.25$ and $|g_{e+h,c}| = 1.94$, see Figure 3b. These lines are provided by double spin-flip processes, in which simultaneously electron and hole spin-flips are involved. This is a rather unusual SFRS process. Double electron spin-flip was found experimentally in 1972 for an exciton interacting with two donor-bound electrons in CdS [62], later in ZnTe [63], and recently for two localized electrons interacting with the same exciton in CdSe colloidal nanoplatelets [54]. The according theoretical consideration can be found in Refs. 64–66. The E_{e-h} and E_{e+h} line shifts are much larger compared to the E_h line, and can therefore be resolved in a larger range of magnetic fields starting from 4 T. We use the difference between the double spin-flip line E_{e+h} and the electron line E_e to evaluate the hole Zeeman splitting vs magnetic field in Figure 3c. Note that the full width at half maximum, taken from the Gaussian fit of the electron spin-flip line, is about 7 times larger (50 μeV) than that for the hole (7 μeV), which indicates a broader electron g -factor dispersion.

Commonly, SFRS signals have a pronounced polarization dependence, caused by the optical selection rules and the involved scattering mechanisms. The spectrum shown in Figure 2b is measured in a cross circularly-polarized configuration with σ^+ polarized excitation and σ^- polarized detection. The other polarization configurations are shown in the Supporting Information, Figure S1a, for both the anti-Stokes and Stokes spec-

tral ranges. Surprisingly, the polarization dependence is weak. Possible reasons for that are discussed in Section II G.

C. Spin-flip Raman scattering in Voigt geometry

In order to determine the in-plane components of the electron and hole g -factors, we perform SFRS measurements in the Voigt geometry, where $\mathbf{B}_V \perp \mathbf{k}$, $\mathbf{B}_V \parallel (a, b)$ and $\theta = 90^\circ$. In Figure 2c the SFRS spectrum for linearly co-polarized excitation and detection in the Voigt geometry at $B_V = 10$ T is shown. This geometry is favorable for SFRS experiments because the spin states are mixed by the perpendicular magnetic field, facilitating an efficient spin-flip process. The comparison of the SFRS spectra in Figures 2b and 2c shows that the SFRS intensity in the Voigt geometry is about five times higher than in the Faraday geometry. In the Voigt geometry the Raman shift of the electron E_e line corresponds to $|g_{e,(a,b)}| = 2.50$, see also Figure 3d. This value is in good agreement with $g_{e,(a,b)} = +2.45 \pm 0.05$ measured by time-resolved Kerr rotation [47]. The slope of the linear fit to the double spin-flip E_{e+h} Raman shift corresponds to $|g_{e+h,(a,b)}| = 1.98$, see Figure 3e. As the E_h line cannot be resolved in this geometry, we calculate its Raman shift from the shift difference between E_{e+h} and E_e . From the data in different magnetic fields we determine the hole g -factor $g_{h,(a,b)} = -0.51$ (Figure 3f). Note that the E_{e-h} line cannot be well detected in Voigt geometry. The SFRS spectra are measured in different configurations of linear polarization, however, a noticeable influence of selection rules is not found, more information is provided in the Supporting Information, Figure S1b.

It is worth pointing out that the amplitude of the spin-flip lines is sensitive to temperature. We show in the Supporting Information, Figure S2, that the electron SFRS line amplitude decreases for temperatures exceeding 5 K and becomes weak above 16 K. We suggest that thermal delocalization of the resident electrons is the mechanism that reduces the efficiency of the SFRS process. The estimated activation energy is about 2.1 meV.

D. Resonance profile of spin-flip Raman scattering

The SFRS intensity has a strong spectral dependence on the laser photon energy as shown in Figure 2e for the E_e line, measured in the Voigt geometry at $B_V = 7$ T. The maximum of the resonance profile coincides with the free exciton energy in the reflectivity spectrum shown in Figure 2d, where also the PL line is given for comparison. This highlights the key role of the exciton in the SFRS process. The exciton resonantly enhances the laser excitation and scattering through the interaction with resident carriers, whose spin-flip Raman shift is measured. Similar results were reported for CdTe/(Cd,Mg)Te quantum wells with a low density of resident electrons [52] and

for singly-charged (In,Ga)As/GaAs quantum dots [53]. In Figure 2d, the electron g -factor is shown as function of the excitation energy. It remains constant across the investigated energy range.

E. g -factors of electrons and holes and their anisotropy

The electron and hole g -factors can be precisely determined from the Raman shifts of the respective lines at different magnetic fields. The results in the close-to-Faraday and Voigt geometries are presented in Figure 3. The electron g -factors are taken from the shift of the E_e line, see Figures 3a,d. Figures 3b,e illustrate the shifts of the double spin-flip lines E_{e+h} and E_{e-h} , which are plotted relative to the E_e line shift. The differences between the E_e and the double spin-flip line shifts correspond to the hole Zeeman splitting, shown in Figures 3c,f. Only in high magnetic fields the E_h shift can be directly measured. The corresponding values of the g -factors are given in the panels of Figure 3 and are also collected in Table I, in which the signs of the g -factors are given.

The anisotropy of the carrier g -factors is inherent for 2D structures and originates from the reduced symmetry of the band structure. For the studied (PEA)₂PbI₄ sample the anisotropy is shown in Figure 3g, where the experimental data for the close-to-Faraday and Voigt geometries are complemented by measurements at the magnetic field tilt angle of $\theta = 22^\circ$. The angular dependence of the g -factor can be described by

$$g(\theta) = \sqrt{(g_c \cos \theta)^2 + (g_{(a,b)} \sin \theta)^2}. \quad (1)$$

The electron g -factor anisotropy measured by TRKR in a vector magnet with smaller steps of the tilt angle can be found in Ref. [47]. It is interesting to note that the anisotropies of g_e and g_h almost compensate each other, so that their sum stays nearly isotropic, $g_{e,c} + g_{h,c} = +1.98$ and $g_{e,(a,b)} + g_{h,(a,b)} = +1.99$. A similar behavior was recently found for bulk CsPbBr₃ crystals [22].

The g -factor of the bright exciton in lead halide perovskites is the sum of the carrier g -factors:

$$g_X = g_e + g_h. \quad (2)$$

Therefore, the exciton g -factor in 2D (PEA)₂PbI₄ should be nearly isotropic despite a clear crystal anisotropy. In fact, g_X may deviate from the relation (2), as some g -factor renormalization can occur at finite carrier k -vectors in the exciton. It is instructive to check this relation for (PEA)₂PbI₄. Here $g_{e,c} + g_{h,c} = +1.98$ can be compared with the $g_{X,c} = +1.6$ measured by magnetoreflectivity (Figure 1c). Indeed, the exciton g -factor is about 0.4 smaller than the sum. We attribute this difference to the large exciton binding energies in the 2D (PEA)₂PbI₄ perovskite. Further model calculations are needed to identify the involved mechanisms.

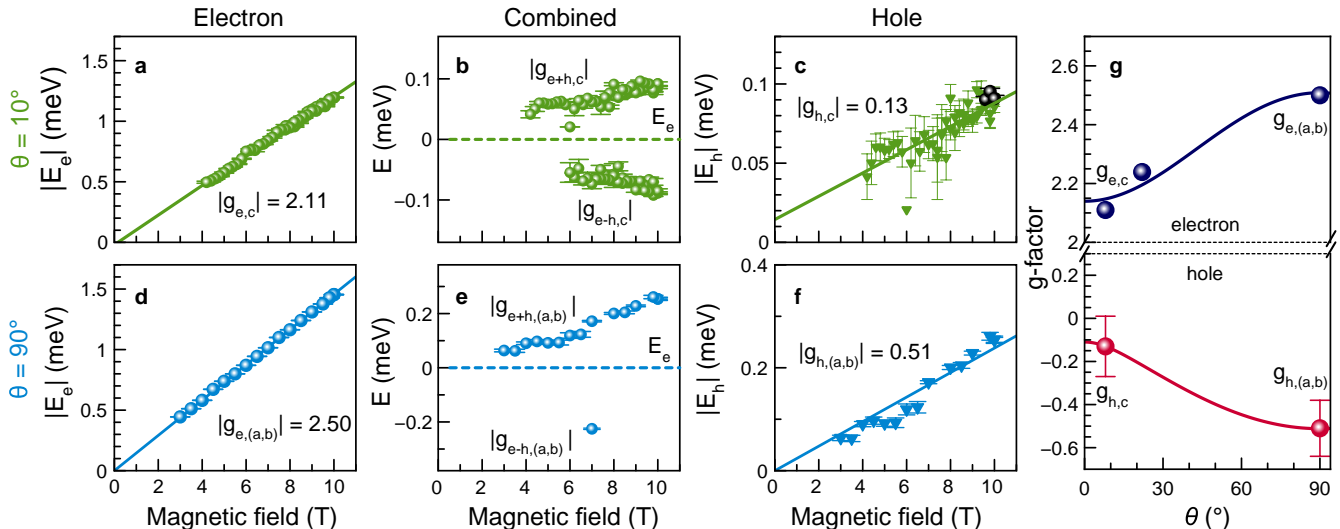


FIG. 3. Raman shifts of the spin-flip lines in magnetic field and evaluated carrier g -factors in $(\text{PEA})_2\text{PbI}_4$. Magnetic field dependences of the anti-Stokes SFRS shifts measured in the close-to-Faraday ($\theta = 10^\circ$) and Voigt ($\theta = 90^\circ$) geometries. (a, d) Electron E_e shift. (b, e) Double spin-flip E_{e+h} and E_{e-h} shifts after subtracting the shift of E_e . (c, f) Hole E_h shift evaluated from the double spin-flip shifts (colored triangles). Black dots in panel (c) give direct measurements of the hole spin-flip shift of the E_h line. In all panels, B -linear fits are shown by the solid lines. (g) g -factor anisotropy for the tilt angle θ tuned between Faraday and Voigt geometry. Lines are fits with Equation (1). All measurements presented here are performed at $T = 1.6$ K with $E_{\text{exc}} = 2.345$ eV laser photon energy using $P = 7.5$ W/cm² excitation power.

	close to Faraday geometry, $\theta = 10^\circ$				Voigt geometry, $\theta = 90^\circ$			
	$g_{e,c}$	$g_{h,c}$	$g_{e-h,c}$	$g_{e+h,c}$	$g_{e,(a,b)}$	$g_{h,(a,b)}$	$g_{e-h,(a,b)}$	$g_{e+h,(a,b)}$
SFRS	+2.11	-0.13	+2.25	+1.94	+2.50	-0.51	+2.93	+1.98
TRKR [47]	+2.05				+2.45			

TABLE I. Overview of the g -factors in the close-to-Faraday geometry ($\theta = 10^\circ$) and in the Voigt geometry ($\theta = 90^\circ$) for $(\text{PEA})_2\text{PbI}_4$ measured by SFRS and time-resolved Kerr rotation [47]. The measurement accuracy is ± 0.05 in all cases. The exciton Zeeman splitting measured by magneto-reflectivity in Faraday geometry is $g_{X,c} = +1.6 \pm 0.1$.

F. Dynamic nuclear polarization

The spin dynamics of electrons and holes in semiconductors are strongly influenced by their hyperfine interaction with the nuclear spin system [67]. In conventional III-V and II-VI semiconductors the conduction band electrons with s-type wave functions have stronger interaction with the nuclei spins compared to the valence band holes with p-type wave functions. This situation is reversed in lead halide perovskites, where the Pb ions greatly contribute to the states around the band gap [21, 60]. Their p-orbitals form the conduction band, while the s-orbitals contribute to the valence band. As a result, the hyperfine interaction of the holes is about 5 times stronger than that of electrons. Similar properties are expected for $(\text{PEA})_2\text{PbI}_4$.

The hyperfine interaction of carriers with the nuclei can be assessed by the effect of dynamic nuclear polarization (DNP). Spin polarized carriers, which can be generated by circularly polarized light using optical orienta-

tion, generate the Knight field (\mathbf{B}_K) that acts as an effective magnetic field on the nuclear spins. Thereby the carrier spin polarization can be transferred to the nuclear spin system, so that it becomes polarized. In turn, the polarized nuclear system induces the Overhauser field (\mathbf{B}_N) that acts on the carrier spins and changes their Zeeman splitting, see scheme in Figure 4d. Details of DNP model description are given in Ref. [21]. Here for simplicity, we will consider only the hole contribution, as we found experimentally that in $(\text{PEA})_2\text{PbI}_4$ the holes are dominant in polarizing the nuclear spins.

The spin polarization of optically oriented holes ($\langle \mathbf{S}_h \rangle$) is transferred to the nuclei and induces the average nuclear spin polarization ($\langle \mathbf{I} \rangle$) given by

$$\langle \mathbf{I} \rangle = l \frac{4I(I+1)}{3} \frac{\mathbf{B}(\mathbf{B} \cdot \langle \mathbf{S}_h \rangle)}{B^2}. \quad (3)$$

Here l is the leakage factor characterizing DNP losses due to relaxation processes and I is the nuclear spin. The nuclear spin polarization builds up along the direction

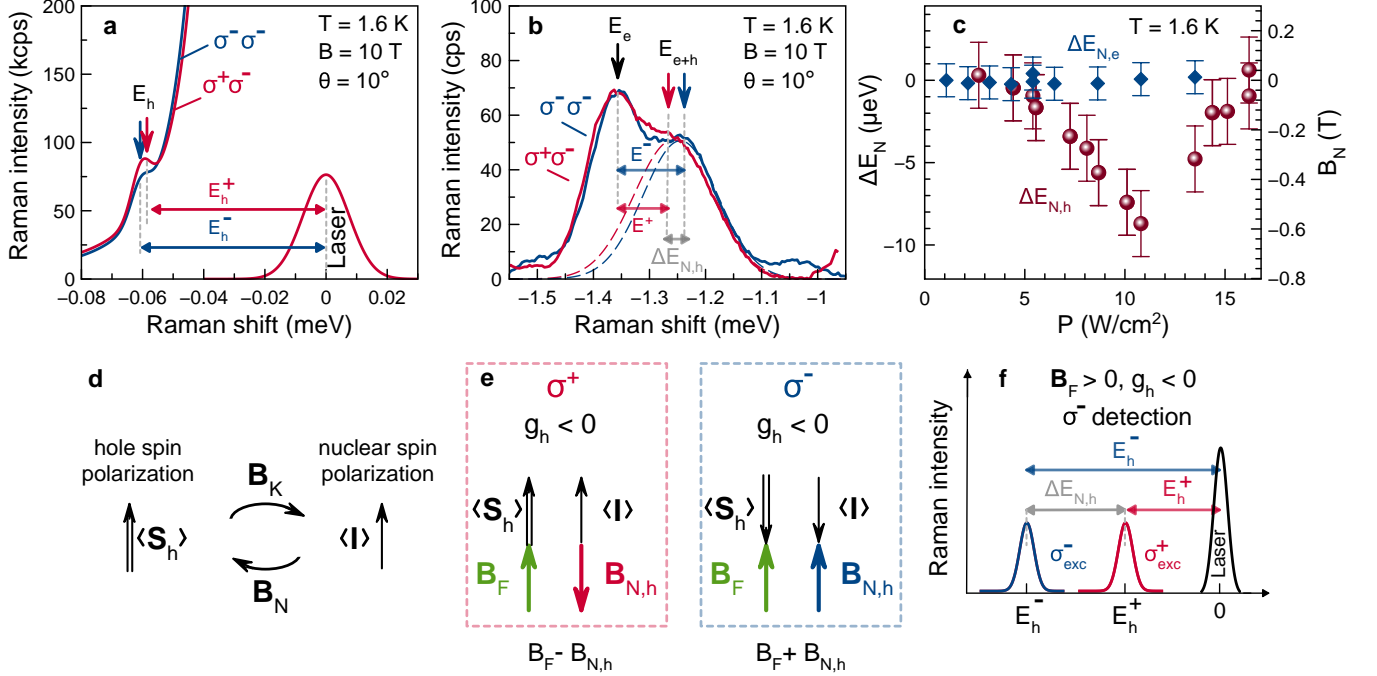


FIG. 4. Dynamic nuclear polarization of holes detected via SFRS in $(\text{PEA})_2\text{PbI}_4$. (a) Raman shift of the hole E_h line measured in $\sigma^- \sigma^-$ and $\sigma^+ \sigma^-$ polarization for $P = 5.1 \text{ W/cm}^2$ excitation power. (b) Raman shift of the electron E_e and double spin-flip E_{e+h} lines measured in different polarizations for $P = 13.5 \text{ W/cm}^2$. (c) Power density dependences of the energy splitting $\Delta E_N = E^+ - E^-$ for the electron and hole shifts from panel (b). Right axis gives the corresponding Overhauser field B_N . (d) Schematic illustration of the hyperfine interaction in a carrier-nuclei spin system. The effective Knight field (B_K) of the spin polarized holes $\langle \mathbf{S}_h \rangle$ acts on the nuclear spin system. The average nuclear spin polarization $\langle \mathbf{I} \rangle$ acts back via the Overhauser field ($B_{N,h}$) on the hole spin. (e) $B_{N,h}$ orientation scheme for $g_h < 0$ with σ^+ or σ^- excitation in an external magnetic field applied in the Faraday geometry. (f) Schematic Raman spectrum highlighting the effect of DNP on the Raman shift. The difference between the Raman line shifts for σ^+ and σ^- excitation is proportional to $2B_{N,h}$.

of projection of $\langle \mathbf{S}_h \rangle$ onto the magnetic field, and therefore its direction can be controlled by the light helicity, which determines the $\langle \mathbf{S}_h \rangle$ orientation. The nuclear spin polarization can be converted into the Overhauser field:

$$\mathbf{B}_{N,h} = \frac{\alpha A_h \langle \mathbf{I} \rangle}{g_h \mu_B} \quad (4)$$

with the positive hyperfine coupling constant for holes $A_h > 0$. Here α is abundance of nuclear isotopes with nonzero spin. The sign of $\mathbf{B}_{N,h}$ is determined by the sign of the hole g -factor, which offers an experimental tool for evaluating the g_h sign. In Figure 4e, diagrams for the orientation possibilities of the magnetic and effective fields as well as the spin polarization are given for σ^+ and σ^- circular polarized excitation. Here, we take $g_h < 0$. Depending on the g_h sign, $\mathbf{B}_{N,h}$ can increase or reduce the hole Zeeman splitting induced by an external magnetic field. Therefore, it changes the spin-flip Raman shift and can be detected experimentally by SFRS. For example, we have demonstrated that for $(\text{In,Ga})\text{As}/\text{GaAs}$ quantum dots [68].

In order to examine the DNP in $(\text{PEA})_2\text{PbI}_4$, we apply the SFRS technique in close-to-Faraday geometry ($\theta = 10^\circ$). The signal is detected in σ^- circular polarization, while the excitation polarization was set to either σ^+ or σ^- . As shown in Figure 4a the shift of the hole spin-flip line is larger in the $\sigma^- \sigma^-$ configuration (we label the shift as E_h^- shown by the blue arrow) than in the $\sigma^+ \sigma^-$ configuration (E_h^+ , the red arrow). Their difference scales with twice the Overhauser field which thus can be extracted from the relation

$$\Delta E_{N,h} = |E_h^+| - |E_h^-| = 2|g_{h,c}| \mu_B B_{N,h}, \quad (5)$$

as sketched in Figure 4f. The difference $\Delta E_{N,h} = |E_h^+| - |E_h^-| = -1.6 \text{ } \mu\text{eV}$ measured at $P = 5.1 \text{ W/cm}^2$ corresponds to $B_{N,h} = -0.11 \text{ T}$ calculated using $|g_{h,c}| = 0.13$. The negative sign of $B_{N,h}$ means that $g_{h,c} < 0$, see Equation (4).

The nuclear-induced shift can be seen even more clearly in the double spin-flip line E_{e+h} , as for it the background contribution of the scattered laser light is strongly

reduced, see Figure 4b. Note that the DNP shift is absent for the electron Zeeman splitting, as the E_e shift is the same for the $\sigma^- \sigma^-$ and $\sigma^+ \sigma^-$ configurations. However, the shift of the E_{e+h} line from E_e varies. For the used excitation density of 13.5 W/cm^2 the energy splitting of these lines amounts to $\Delta E_{N,h} = -5.5 \text{ } \mu\text{eV}$ and, therefore, to $B_{N,h} = -0.36 \text{ T}$.

The excitation density dependences of $\Delta E_N(P)$ and $B_N(P)$ for electrons and holes are shown in Figure 4c. As already noted, any effect on the electrons is absent, reflecting the expected weak hyperfine interaction in the 2D $(\text{PEA})_2\text{PbI}_4$ perovskite. The energy splitting is pronounced for holes, for which the $\Delta E_{N,h}$ value increases up to $-8.7 \text{ } \mu\text{eV}$, which corresponds to $B_{N,h} = -0.6 \text{ T}$ at $P = 10.5 \text{ W/cm}^2$. For a further excitation density increase the energy splitting becomes weaker, which we assign to heating of the nuclear spin system.

The results of this section show that the SFRS technique is a valuable tool for providing insight into the central spin problem of a carrier spin placed in a nuclear spin bath in 2D perovskite materials and also for studying perovskite bulk crystals and nanocrystals.

G. Discussion

Let us discuss the mechanisms that can be responsible for the observed spin-flip processes. Recently a detailed theoretical analysis of the spin-flip Raman scattering processes involving excitons and resident charge carriers in perovskite semiconductors was published [65]. The model considerations were made for bulk perovskites with cubic symmetry. Three mechanisms for the observation of carrier spin-flips were suggested that can explain both the single and double spin-flip processes. The first mechanism is the resonant excitation of a localized exciton, followed by its exchange interaction with a resident electron and/or hole. The second mechanism involves a biexciton as an intermediate state of the SFRS. In this case, spin-flip shifts by the energies of E_{e+h} and $E_{e+h}/2$ are expected, but the process with E_{e-h} is forbidden. We observe, however, in the experiment the E_{e-h} process, which allows us to exclude the biexciton scenario. The third mechanism is the direct excitation of propagating exciton-polaritons, their scattering on resident carriers, and the conversion of the polaritons into secondary photons at the sample boundary. In 2D perovskites the semiconductor layers are electronically decoupled from each other which prevents exciton-polariton motion along the c -axis. Therefore, we suggest that the exciton-polariton mechanism can be neglected for them.

Our experimental results on the spectral dependence of the SFRS intensity clearly show the exciton involvement. In turn, the Raman shift values and their anisotropy allow us to refer them to resident carriers, which interact with the exciton acting as a mediator of the SFRS. The considerations of Ref. 65 predict pronounced polarization dependencies for the carrier spin-flip lines. So far, the

reason why such dependencies are not observed here is unclear, see the Supporting Information, Figure S1. Future analysis accounting for the reduced symmetry and mixing of the bright exciton states in 2D perovskites might clarify this property. Note that the 2D perovskites are similar 2D CdSe colloidal nanoplatelets, but for the nanoplatelets we do observe pronounced polarization dependences of the spin-flip lines [54]. The SFRS theory for the CdSe nanoplatelets is presented in Ref. 66. Here, the violation of polarization selection rules caused by the in-plane anisotropy of the nanoplatelets, which induces exciton mixing and splitting, and by the finite Zeeman splitting of the intermediate state were analyzed.

We have measured the exciton g -factor in $(\text{PEA})_2\text{PbI}_4$ of $g_{X,c} = +1.6$ from the exciton Zeeman splitting in magneto-reflectivity, see Figure 1c. It is in agreement with reported experimental data for 2D perovskite excitons measured in pulsed magnetic fields up to 60 T, where either magneto-transmission or magneto-reflectivity were used. The exciton g -factor of about 1.2 was measured for $(\text{PEA})_2\text{PbI}_4$ [37]. For the similar 2D perovskite $(\text{C}_6\text{H}_{13}\text{NH}_3)_2\text{PbI}_4$ it amounts to about 1.5 [69] and +1.80 [34]. For $(\text{C}_{10}\text{H}_{21}\text{NH}_3)_2\text{PbI}_4$ it is +1.42 [35], and for the halogen substitution for Br in $(\text{C}_4\text{H}_9\text{NH}_3)_2\text{PbBr}_4$ the g -factor is +1.2 [36].

Another type of spin-flip Raman scattering process was observed in the $(\text{C}_4\text{H}_9\text{NH}_3)_2\text{PbBr}_4$ 2D perovskite [33]. These experiments were performed at zero magnetic field, where the Raman shift by the large value of $28 - 32 \text{ meV}$ arises from the scattering of a bright exciton with parallel electron and hole spins into a dark exciton state with antiparallel spins. This shift corresponds to the bright-dark exchange splitting of the excitons and not to the Zeeman splitting of their states.

III. CONCLUSIONS

We have investigated the spin properties of two-dimensional $(\text{PEA})_2\text{PbI}_4$ perovskites using spin-flip Raman scattering. We have found spin-flip signals from resident electrons and holes, as well as their combinations. This has allowed us to measure the Landé factors and their anisotropy. The anisotropy of the electron and hole g -factors is complementary, so that their sum corresponding to the bright exciton g -factor remains isotropic. Also, hyperfine hole-nuclei interaction is demonstrated in 2D perovskites by means of the dynamic nuclear polarization. Due to the small g -factor of the hole, we were able to achieve an Overhauser field value of $B_{N,h} = 0.6 \text{ T}$. The direction of $\mathbf{B}_{N,h}$ allows us to unambiguously determine the negative sign of the hole g -factor. We are convinced that similar effects as those observed can manifest themselves in the large class of 2D lead halide perovskites with different numbers of layers, as well as in perovskites with various organic cations.

IV. EXPERIMENTAL SECTION

A. Samples

We studied Ruddlesden-Popper type two-dimensional $(\text{PEA})_2\text{PbI}_4$ perovskites that consist of a stack of monolayers formed by corner-shared PbI_6 octahedra. The monolayers are separated by van der Waals-bonded pairs of PEA [phenethylammonium $(\text{C}_6\text{H}_5)_2\text{C}_2\text{H}_4\text{NH}_3$] molecules. Details of the synthesis are given in the Supporting Information, S1, and in Ref. 47. Due to the quantum confinement of electrons and holes the band gap energy of $(\text{PEA})_2\text{PbI}_4$ is 2.608 eV at $T = 2$ K [37]. This value considerably exceeds the band gap energy of APbI_3 lead iodine archetype bulk crystals with $E_g = 1.5 - 1.7$ eV, where $A = \text{Cs}^+$, MA^+ , or FA^+ . The reduced dimensionality and the dielectric enhancement effect, provided by the contrast in dielectric constants between the perovskite monolayers and the PEA, strongly increase the exciton binding energy in $(\text{PEA})_2\text{PbI}_4$ to 260 meV [37, 41] in comparison to 16 meV in bulk MAPbI_3 perovskite [55].

B. Experimental details

1. Spin-flip Raman scattering (SFRS) spectroscopy

The SFRS technique enables one to directly measure the Zeeman splitting of the electron and hole spins from the spectral shift of the scattered light from the laser photon energy. Resonant excitation of the exciton strongly increases the SFRS signals, allowing one to measure resident electrons and holes interacting with an exciton. For optical excitation we used a tunable single-frequency continuous wave Ti:Sapphire laser (Matisse DS) equipped with a MixTrain module from SIRAH. The emitted photon energy was tuned around 530 nm (spectral range 2.33 – 2.36 eV), provided by the sum frequency of the Ti:Sapphire laser operating around 720 nm and a fiber laser emitting at 1950 nm. The actual wavelength was measured and monitored by a fiber-coupled high-resolution wavemeter (HighFinesse WSU). The laser power after the MixTrain module was generally set to 0.7 mW. The diameter of the laser spot on the sample was 180 μm in diameter resulting in an excitation density of $P = 2.75$ W/cm², if not specified otherwise. The linear or circular polarizations of the laser beam and the Raman signal were set and analyzed by combinations of $\lambda/2$ or $\lambda/4$ wave plates and a Glan-Thompson prism, positioned in the excitation and detection paths. The linear polarizations are denoted as V (vertical) and H (horizontal), and the circular polarizations as σ^+ and σ^- .

The Raman signals were measured in backscattering geometry. The light scattered from the sample was dispersed by a 1 m double monochromator (Yobin-Yvon

U1000) equipped with a Peltier-cooled GaAs photomultiplier providing a spectral resolution of 0.8 μeV . This allows us to measure g -factors with an accuracy of 0.05. To protect the photomultiplier from the highly intense laser light, a neutral density filter is placed in the detection path while recording the laser. The SFRS measurements were performed at the low temperature of $T = 1.6$ K with the sample immersed in pumped liquid helium. Magnetic fields up to 10 T generated by a superconducting split-coil solenoid were applied. In Figure 2a the used experimental geometries are shown. The sample axes a and b are in-plane, while the c -axis is out-of-plane. In the Faraday geometry, the magnetic field is parallel to the light wave vector k and to the c -axis ($\mathbf{B}_F \parallel \mathbf{k}$, $\mathbf{B}_F \parallel c$ and $\theta = 0^\circ$). In the Voigt geometry the field is perpendicular to these vectors ($\mathbf{B}_V \perp \mathbf{k}$, $\mathbf{B}_V \parallel (a, b)$ and $\theta = 90^\circ$). In our experiments we did not distinguish between the orientations of the a - and b -axes, and therefore the measured values are averaged over their random orientations, while the differences between the two axes are not expected to be large. The angle θ between the c -axis and the magnetic field specifies the tilt of the field directions as shown in the bottom diagram, where $\mathbf{k} \parallel \mathbf{B}$ is kept.

2. Photoluminescence (PL)

Nonresonant continuous wave excitation with the photon energy of 2.412 eV and an excitation density of $P = 10.8$ W/cm² was used for the PL measurements performed at $T = 1.6$ K. The PL was detected by the same 1 m double monochromator (U1000) and GaAs photomultiplier, as in the SFRS measurements.

3. Time-resolved photoluminescence (TRPL)

For the TRPL measurements, a pulsed excitation laser was used (pulse duration of 10 ns, pulse repetition rate of 800 Hz, photon energy of 3.493 eV, and excitation density of $P = 3$ W/cm²). The PL was detected again with the Peltier-cooled GaAs photomultiplier coupled to the U1000. The time resolution of the recombination dynamics was provided by a time-of-flight electronic board (Fast ComTec MCS6A), which has a nominal time resolution of 100 ps. In our experiment the time resolution of 10 ns was limited by the laser pulse duration.

Supporting Information

Correspondence and requests for material should be addressed to D.R.Y. (dmitri.yakovlev@tu-dortmund.de).

Acknowledgements

We are thankful to A. V. Rodina, E. L. Ivchenko, M. O. Nestoklon, M. M. Glazov, and I. V. Kalitukha for fruitful discussions. We acknowledge the financial support by the Deutsche Forschungsgemeinschaft in the frame of

the Priority Programme SPP 2196 (Project YA 65/26-1) and the International Collaboration Research Center TRR160 (Projects A1 and B2). The work of O.H. and M.V.K. was financially supported by the Swiss National Science Foundation (grant agreement 186406, funded in conjunction with SPP2196 through DFG-SNSF bilateral program) and by the ETH Zürich through the ETH+ Project SynMatLab: Laboratory for Multiscale Materials Synthesis.

Competing interests

The authors declare no competing interests.

ORCID

Carolyn Harkort: 0000-0003-1975-9773
 Dennis Kudlacik: 0000-0001-5473-8383
 Nataliia E. Kopteva: 0000-0003-0865-0393
 Dmitri R. Yakovlev: 0000-0001-7349-2745
 Marek Karzel: 0000-0002-1939-5191
 Erik Kirstein: 0000-0002-2549-2115
 Oleh Hordiichuk: 0000-0001-7679-4423
 Maksym V. Kovalenko: 0000-0002-6396-8938
 Manfred Bayer: 0000-0002-0893-5949

-
- [1] *Halide Perovskites for Photonics*, eds. A. Vinattieri, G. Giorgi, AIP Publishing, Melville, New York, **2021**.
- [2] *Hybrid Organic Inorganic Perovskites: Physical Properties and Applications*, eds. Z. V. Vardeny, M. C. Beard, World Scientific, **2022**. Vol. 4 on *Hybrid Organic Inorganic Perovskite Applications*.
- [3] A. K. Jena, A. Kulkarni, T. Miyasaka, Halide perovskite photovoltaics: Background, status, and future prospects. *Chem. Rev.* **2019**, *5*, 3036–3103.
- [4] C. Hansell, L. Fleet, M. Lee, E. Couderc, G. Tregnago, L. Martiradonna, O. Bubnova, O. Graydon, J. P. Kraack, B. Liu, M. Citroni, G. Graziano, A. Stoddart, Perovskites for optoelectronics, **2019**. <https://www.nature.com/collections/fnnxcznnbb/content/reviews>.
- [5] L. Mao, C. C. Stoumpos, M. G. Kanatzidis, Two-dimensional hybrid halide Perovskites: principles and promises. *J. Am. Chem. Soc.* **2018**, *141*, 1171.
- [6] J.-C. Blancon, J. Even, C. C. Stoumpos, M. G. Kanatzidis, A. D. Mohite, Semiconductor physics of organic–inorganic 2D halide perovskites. *Nature Nanotechnology* **2020**, *15*, 969.
- [7] R. L. Z. Hoye, J. Hidalgo, R. A. Jagt, J.-P. Correa-Baena, T. Fix, J. L. MacManus-Driscoll, The Role of Dimensionality on the Optoelectronic Properties of Oxide and Halide Perovskites, and their Halide Derivatives. *Advanced Energy Materials* **2022**, *12*, 02100499.
- [8] N. Wang, L. Cheng, R. Ge, S. Zhang, Y. Miao, W. Zou, C. Yi, Y. Sun, Y. Cao, R. Yang, Y. Wei, Q. Guo, Y. Ke, M. Yu, Y. Jin, Y. Liu, Q. Ding, D. Di, L. Yang, G. Xing, H. Tian, C. Jin, F. Gao, R. H. Friend, J. Wang, W. Huang, Perovskite light-emitting diodes based on solution-processed self-organized multiple quantum wells. *Nature Photonics* **2020**, *10*, 699.
- [9] K. Lempicka-Mirek, M. Król, H. Sigurdsson, A. Wincukiewicz, P. Morawiak, R. Mazur, M. Muszyński, W. Piecek, P. Kula, T. Stefaniuk, M. Kamińska, L. De Marco, P. G. Lagoudakis, D. Ballarini, D. Sanvitto, J. Szczytko, B. Pietka, Electrically tunable Berry curvature and strong light-matter coupling in birefringent perovskite microcavities at room temperature. *Science Advances* **2022**, *8*, eabq7533.
- [10] X. Zhang, R. Munir, Z. Xu, Y. Liu, H. Tsai, W. Nie, J. Li, T. Niu, D.-M. Smilgies, M. G. Kanatzidis, A. D. Mohite, K. Zhao, A. Amassian, S. F. Liu, Phase Transition Control for High Performance Ruddlesden–Popper Perovskite Solar Cells. *Advanced Materials* **2018**, *30*, 1707166.
- [11] P. Cheng, Z. Xu, J. Li, Y. Liu, Y. Fan, L. Yu, D.-M. Smilgies, C. Müller, K. Zhao, S. F. Liu, Highly Efficient Ruddlesden–Popper Halide Perovskite $\text{PA}_2\text{MA}_4\text{Pb}_5\text{I}_{16}$ Solar Cells. *ACS Energy Letters* **2018**, *3*, 1975.
- [12] S. Sidhik, Y. Wang, W. Li, H. Zhang, X. Zhong, A. Agrawal, I. Hadar, I. Spanopoulos, A. Mishra, B. Traoré, M. H. K. Samani, C. Katan, A. B. Marciel, J.-C. Blancon, J. Even, A. Kahn, M. G. Kanatzidis, A. D. Mohite, High-phase purity two-dimensional perovskites with 17.3% efficiency enabled by interface engineering of hole transport layer. *Cell Reports Physical Science* **2021**, *2*, 100601.
- [13] E. A. Muljarov, S. G. Tikhodeev, N. A. Gippius, T. Ishihara, Excitons in self-organized semiconductor/insulator superlattices: PbI-based perovskite compounds. *Phys. Rev. B* **1995**, *51*, 14370; L. V. Kulik, V. D. Kulakovskii, M. Bayer, A. Forchel, N. A. Gippius, and S. G. Tikhodeev, Dielectric enhancement of excitons in near-surface quantum wells *Phys. Rev. B* **1996**, *54*, 2335.
- [14] J.-C. Blancon, A. V. Stier, H. Tsai, W. Nie, C. C. Stoumpos, B. Traoré, L. Pedesseau, M. Kepenekian, F. Katsutani, G. T. Noe, J. Kono, S. Tretiak, S. A. Crooker, C. Katan, M. G. Kanatzidis, J. J. Crochet, J. Even, A. D. Mohite, Scaling law for excitons in 2D perovskite quantum wells. *Nature Communications* **2018**, *9*, 2254.
- [15] T. Ishihara, J. Takahashi, T. Goto, Exciton state in two-dimensional perovskite semiconductor $(\text{C}_{10}\text{H}_{21}\text{NH}_3)_2\text{PbI}_4$. *Solid State Commun.* **1989**, *69*, 933.
- [16] T. Ishihara, J. Takahashi, T. Goto, Optical properties due to electronic transitions in two-dimensional semiconductors $(\text{C}_n\text{H}_{(2n+1)}\text{NH}_3)\text{PbI}_4$. *Phys. Rev. B* **1990**, *42*, 11099.
- [17] G. Wang, A. Chernikov, M. M. Glazov, T. F. Heinz, X. Marie, T. Amand, B. Urbaszek, Colloquium: Excitons in atomically thin transition metal dichalcogenides. *Rev. Mod. Phys.* **2018**, *90*, 021001.
- [18] J. Even, L. Pedesseau, C. Katan, M. Kepenekian, J.-S. Lauret, D. Saporì, E. Deleporte, Solid-state physics perspective on hybrid perovskite semiconductors. *J. Phys.*

- Chem.* **2015**, *119*, 10161.
- [19] C. Katan, N. Mercier, J. Even, Quantum and dielectric confinement effects in lower-dimensional hybrid perovskite semiconductors. *Chem. Rev.* **2019**, *119*, 3140.
- [20] Z. Yu, Effective-mass model and magneto-optical properties in hybrid perovskites. *Sci. Rep.* **2016**, *6*, 28576.
- [21] E. Kirstein, D. R. Yakovlev, M. M. Glazov, E. Evers, E. A. Zhukov, V. V. Belykh, N. E. Kopteva, D. Kudlacik, O. Nazarenko, D. N. Dirin, M. V. Kovalenko, M. Bayer, Lead-dominated hyperfine interaction impacting the carrier spin dynamics in halide perovskites. *Advanced Materials* **2022**, *34*, 2105263.
- [22] E. Kirstein, D. R. Yakovlev, M. M. Glazov, E. A. Zhukov, D. Kudlacik, I. V. Kalitukha, V. F. Sapega, G. S. Dimitriev, M. A. Semina, M. O. Nestoklon, E. L. Ivchenko, N. E. Kopteva, D. N. Dirin, O. Nazarenko, M. V. Kovalenko, A. Baumann, J. Höcker, V. Dyakonov, M. Bayer, The Landé factors of electrons and holes in lead halide perovskites: universal dependence on the band gap. *Nature Communications* **2022**, *13*, 3062.
- [23] *Hybrid Organic Inorganic Perovskites: Physical Properties and Applications*, eds. Z. V. Vardeny, M. C. Beard, World Scientific, **2022**. Vol. 3 on *Spin Response of Hybrid Organic Inorganic Perovskites*.
- [24] D. Giovanni, H. Ma, J. Chua, M. Grätzel, R. Ramesh, S. Mhaisalkar, N. Mathews, T. C. Sum, Highly Spin-Polarized Carrier Dynamics and Ultralarge Photoinduced Magnetization in $\text{CH}_3\text{NH}_3\text{PbI}_3$ Perovskite Thin Films. *Nano Letters* **2015**, *15*, 1553.
- [25] M. O. Nestoklon, S. V. Goupalov, R. I. Dzhioev, O. S. Ken, V. L. Korenev, Yu. G. Kusrayev, V. F. Sapega, C. de Weerd, L. Gomez, T. Gregorkiewicz, J. Lin, K. Suenaga, Y. Fujiwara, L. B. Matyushkin, I. N. Yassievich, Optical orientation and alignment of excitons in ensembles of inorganic perovskite nanocrystals. *Phys. Rev. B* **2018**, *97*, 235304.
- [26] R. Wang, S. Hu, X. Yang, X. Yan, H. Li, C. Sheng, Circularly polarized photoluminescence and Hanle effect measurements of spin relaxation in organic-inorganic hybrid perovskite films. *J. Mater. Chem. C* **2018**, *6*, 2989.
- [27] J. Wang, C. Zhang, H. Liu, R. McLaughlin, Y. Zhai, S. R. Vardeny, X. Liu, S. McGill, D. Semenov, H. Guo, R. Tsuchikawa, V. V. Deshpande, D. Sun, Z. V. Vardeny, Spin-optoelectronic devices based on hybrid organic-inorganic trihalide perovskites. *Nature Communications* **2019**, *10*, 129.
- [28] C. Zhang, D. Sun, C.-X. Sheng, Y. X. Zhai, K. Mielczarek, A. Zakhidov, Z. V. Vardeny, Magnetic field effects in hybrid perovskite devices. *Nature Physics* **2015**, *11*, 427.
- [29] D. Canneson, E. V. Shornikova, D. R. Yakovlev, T. Rogge, A. A. Mitioglu, M. V. Ballottin, P. C. M. Christianen, E. Lhuillier, M. Bayer, L. Biadala, Negatively Charged and Dark Excitons in CsPbBr_3 Perovskite Nanocrystals Revealed by High Magnetic Fields. *Nano Letters* **2017**, *17*, 6177.
- [30] C. Zhang, D. Sun, Z.-G. Yu, C.-X. Sheng, S. McGill, D. Semenov, Z. V. Vardeny, Field-induced spin splitting and anomalous photoluminescence circular polarization in $\text{CH}_3\text{NH}_3\text{PbI}_3$ films at high magnetic field. *Phys. Rev. B* **2018**, *97*, 134412.
- [31] P. Odenthal, W. Talmadge, N. Gundlach, R. Wang, C. Zhang, D. Sun, Z.-G. Yu, Z. V. Vardeny, Y. S. Li, Spin-polarized exciton quantum beating in hybrid organic-inorganic perovskites. *Nature Physics* **2017**, *13*, 894.
- [32] V. V. Belykh, D. R. Yakovlev, M. M. Glazov, P. S. Grigoryev, M. Hussain, J. Rautert, D. N. Dirin, M. V. Kovalenko, M. Bayer, Coherent spin dynamics of electrons and holes in CsPbBr_3 perovskite crystals. *Nature Communications* **2019**, *10*, 673.
- [33] K. Ema, K. Umeda, M. Toda, C. Yajima, Y. Arai, H. Kunugita, D. Wolverson, J. J. Davies, Huge exchange energy and fine structure of excitons in an organic-inorganic quantum well material. *Phys. Rev. B* **2006**, *73*, 241310(R).
- [34] T. Kataoka, T. Kondo, R. Ito, S. Sasaki, K. Uchida, N. Miura, Magneto-optical study on excitonic spectra in $(\text{C}_6\text{H}_{13}\text{NH}_3)_2\text{PbI}_4$. *Phys. Rev. B* **1993**, *47*, 2010.
- [35] M. Hirasawa, T. Ishihara, T. Goto, S. Sasaki, K. Uchida, N. Miura, Magnetoreflexion of the lowest exciton in a layered perovskite-type compound $(\text{C}_{10}\text{H}_{21}\text{NH}_3)_2\text{PbI}_4$. *Solid State Commun.* **1993**, *86*, 479.
- [36] K. Tanaka, T. Takahashi, T. Kondo, K. Umeda, K. Ema, T. Umebayashi, K. Asai, K. Uchida, N. Miura, Electronic and excitonic structures of inorganic-organic perovskite-type quantum-well crystal $(\text{C}_4\text{H}_9\text{NH}_3)_2\text{PbBr}_4$. *Jap. J. Appl. Phys.* **2005**, *44*, 5923.
- [37] M. Dyksik, H. Duim, X. Zhu, Z. Yang, M. Gen, Y. Kohama, S. Adjokatse, D. K. Maude, M. A. Loi, D. A. Egger, M. Baranowski, P. Plochocka, Broad Tunability of Carrier Effective Masses in Two-Dimensional Halide Perovskites. *ACS Energy Letters* **2020**, *5*, 3609.
- [38] M. Dyksik, H. Duim, D. K. Maude, M. Baranowski, M. A. Loi, P. Plochocka, Brightening of dark excitons in 2D perovskites. *Science Advances* **2021**, *7*, eabk0904.
- [39] T. T. H. Do, A. G. del Águila, D. Zhang, J. Xing, S. Liu, M. A. Prosnikov, W. Gao, K. Chang, P. C. M. Christianen, Q. Xiong, Bright Exciton Fine-Structure in Two-Dimensional Lead Halide Perovskites. *Nano Letters* **2020**, *20*, 5141.
- [40] A. Surrente, M. Baranowski, P. Plochocka, Perspective on the physics of two-dimensional perovskites in high magnetic field. *Appl. Phys. Lett.* **2021**, *118*, 170501.
- [41] M. Baranowski, M. Dyksik, P. Plochocka, 2D metal halide perovskites: a new fascinating playground for exciton fine structure investigations. *Scientiae Radices* **2022**, *1*, 3.
- [42] D. Giovanni, W. K. Chong, Y. Y. F. Liu, H. A. Dewi, T. Yin, Y. Lekina, Z. X. Shen, N. Mathews, C. K. Gan, T. C. Sum, Coherent Spin and Quasiparticle Dynamics in Solution-Processed Layered 2D Lead Halide Perovskites. *Advanced Science* **2018**, *5*, 1800664.
- [43] X. Pan, H. Liu, U. Huynh, Z. V. Vardeny, Magneto-electroluminescence response in 2D and 3D hybrid organic-inorganic perovskite light emitting diodes. *J. Chem. Phys.* **2020**, *152*, 044714.
- [44] X. Chen, H. Lu, K. Wang, Y. Zhai, V. Lunin, P. C. Sercel, M. C. Beard, Tuning Spin-Polarized Lifetime in Two-Dimensional Metal-Halide Perovskite through Exciton Binding Energy. *J. ACS* **2021**, *143*, 19438.
- [45] S. A. Bourelle, R. Shivanna, F. V. A. Camargo, S. Ghosh, A. J. Gillett, S. P. Senanayak, S. Feldmann, L. Eyre, A. Ashoka, T. W. J. van de Goor, H. Abolins, T. Winkler, G. Cerullo, R. H. Friend, F. Deschler, How exciton interactions control spin-depolarization in layered hybrid perovskites. *Nano Lett.* **2020**, *20*, 5678.
- [46] S. A. Bourelle, F. V. A. Camargo, S. Ghosh, T. Neumann, T. W. J. van de Goor, R. Shivanna, T. Winkler, G. Cerullo, F. Deschler, Optical control of exciton spin dy-

- namics in layered metal halide perovskites via polaronic state formation. *Nature Communications* **2022**, *13*, 3320.
- [47] E. Kirstein, E. A. Zhukov, D. R. Yakovlev, N. E. Kopteva, C. Harkort, D. Kudlacik, O. Hordiichuk, M. V. Kovalenko, M. Bayer, Coherent spin dynamics of electrons in two-dimensional (PEA)₂PbI₄ perovskites. *Nano Letters* **2023**, *23*, 205.
- [48] D. G. Thomas, J. J. Hopfield, Spin-flip Raman scattering in cadmium sulfide. *Phys. Rev.* **1968**, *175*, 1021.
- [49] H. G. Häfele, chapter on Spin-Flip Raman Scattering in *Landau Level Spectroscopy*, Eds. G. Landwehr and E. I. Rashba, vol. 27, pp. 208–275, Elsevier, Amsterdam, 1991.
- [50] V. F. Sapega, T. Ruf, M. Cardona, K. Ploog, E. L. Ivchenko, D. N. Mirlin, Resonant Raman scattering due to bound-carrier spin flip in GaAs/Al_xGa_{1-x}As quantum wells. *Phys. Rev. B* **1994**, *50*, 2510.
- [51] A. A. Sirenko, T. Ruf, M. Cardona, D. R. Yakovlev, W. Ossau, A. Waag, G. Landwehr, Electron and hole *g* factors measured by spin-flip Raman scattering in CdTe/Cd_{1-x}Mg_xTe single quantum wells. *Phys. Rev. B* **1997**, *56*, 2114.
- [52] J. Debus, D. Dunker, V. F. Sapega, D. R. Yakovlev, G. Karczewski, T. Wojtowicz, J. Kossut, M. Bayer, Spin-flip Raman scattering of the neutral and charged excitons confined in a CdTe/(Cd,Mg)Te quantum well. *Phys. Rev. B* **2013**, *87*, 205316.
- [53] J. Debus, V. F. Sapega, D. Dunker, D. R. Yakovlev, D. Reuter, A. D. Wieck, and M. Bayer, Spin-flip Raman scattering of the resident electron in singly charged (In,Ga)As/GaAs quantum dot ensembles. *Phys. Rev. B* **2014**, *90*, 235404.
- [54] D. Kudlacik, V. F. Sapega, D. R. Yakovlev, I. V. Kalitukha, E. V. Shornikova, A. V. Rodina, E. L. Ivchenko, G. S. Dimitriev, M. Nasilowski, B. Dubertret, M. Bayer, Single and double electron spin-flip Raman scattering in CdSe colloidal nanoplatelets. *Nano Lett.* **2020**, *20*, 517.
- [55] K. Galkowski, A. Mitioglu, A. Miyata, P. Plochocka, O. Portugall, G. E. Eperon, J. Tse-Wei Wang, T. Stergiopoulos, S. D. Stranks, H. J. Snaith, and R. J. Nicholas, Determination of the exciton binding energy and effective masses for methylammonium and formamidinium lead tri-halide perovskite semiconductors. *Energy Environ. Sci.* **2016**, *9*, 962.
- [56] K. Posmyk, N. Zawadzka, M. Dyksik, A. Surrente, D. K. Maude, T. Kazimierzuk, A. Babinski, M. R. Molas, W. Paritmongkol, M. Maczka, W. A. Tisdale, P. Plochocka, M. Baranowski, Quantification of exciton fine structure splitting in a two-dimensional perovskite compound. *J. Phys. Chem. Lett.* **2022**, *13*, 4463.
- [57] T. Thu Ha Do, A. Granados del Águila, J. Xing, S. Liu, Q. Xiong, Direct and indirect exciton transitions in two-dimensional lead halide perovskite semiconductors. *J. Chem. Phys.* **2020**, *153*, 064705.
- [58] S. Kahmann, H. Duim, H.-H. Fang, M. Dyksik, S. Adjokatse, M. Rivera Medina, M. Pitaro, P. Plochocka, M. A. Loi, Photophysics of two-dimensional perovskites – learning from metal halide substitution. *Adv. Funct. Mater.* **2021**, *31*, 2103778.
- [59] H.-H. Fang, J. Yang, S. Adjokatse, E. Tekelenburg, M. E. Kamminga, H. Duim, J. Ye, G. R. Blake, J. Even, M. A. Loi, Band-edge exciton fine structure and exciton recombination dynamics in single crystals of layered hybrid perovskites. *Adv. Funct. Mater.* **2020**, *30*, 1907979.
- [60] E. Kirstein, D. R. Yakovlev, E. A. Zhukov, J. Höcker, V. Dyakonov, M. Bayer, Spin dynamics of electrons and holes interacting with nuclei in MAPbI₃ perovskite single crystals. *ACS Photonics* **2022**, *9*, 1375.
- [61] T. Neumann, S. Feldmann, P. Moser, A. Delhomme, J. Zerhoch, T. van de Goor, S. Wang, M. Dyksik, T. Winkler, J. J. Finley, P. Plochocka, M. S. Brandt, C. Faugeras, A. V. Stier, F. Deschler, Manganese doping for enhanced magnetic brightening and circular polarization control of dark excitons in paramagnetic layered hybrid metal-halide perovskites. *Nature Communications* **2021**, *12*, 3489.
- [62] J. F. Scott, T. C. Damen, Anomalous double spin-flip Raman scattering in CdS, and a visible spin-flip laser. *Phys. Rev. Lett.* **1972**, *29*, 107.
- [63] Y. Oka, M. Cardona, Resonant spin-flip Raman scattering on donor and acceptor states in ZnTe. *Phys. Rev. B* **1981**, *293*, 4129.
- [64] E. N. Economou, J. Ruvalds, K. L. Ngai, Theory of multiple spin-flip Raman scattering in semiconductors. *Phys. Rev. Lett.* **1972**, *29*, 110.
- [65] A. V. Rodina, E. L. Ivchenko, Theory of resonant Raman scattering due to spin flips of resident charge carriers and excitons in perovskite semiconductors. *Phys. Rev. B* **2022**, *106*, 245202.
- [66] A. V. Rodina, E. L. Ivchenko, Theory of single and double electron spin-flip Raman scattering in semiconductor nanoplatelets. *Phys. Rev. B* **2020**, *102*, 235432.
- [67] *Optical Orientation*, eds. F. Meier and B. P. Zakharchenya. Elsevier Science Publishers, **1984**.
- [68] J. Debus, D. Kudlacik, V. F. Sapega, D. Dunker, P. Bohn, F. Paßmann, D. Braukmann, J. Rautert, D. R. Yakovlev, D. Reuter, A. D. Wieck, and M. Bayer, Nuclear spin polarization in the electron spin-flip Raman scattering of singly charged (In,Ga)As/GaAs quantum dots. *Phys. Rev. B* **2015**, *92*, 195421.
- [69] M. Baranowski, S. J. Zelewski, M. Kepenekian, B. Traore, J. M. Urban, A. Surrente, K. Galkowski, D. K. Maude, A. Kuc, E. P. Booker, R. Kudrawiec, S. D. Stranks, P. Plochocka, Phase-transition-induced carrier mass enhancement in 2D Ruddlesden-Popper perovskites. *ACS Energy Lett.* **2019**, *4*, 2386.

Supporting Information:

Spin-flip Raman scattering on electrons and holes in two-dimensional (PEA)₂PbI₄ perovskites

S1. PREPARATION OF THE (PEA)₂PbI₄ THIN FILMS

The monolayer-thick 2D hybrid organic-inorganic lead halide perovskites have the stoichiometry $A_m\text{PbX}_4$, with the halide X of the corner shared $[\text{PbX}_6]^{4-}$ octahedra forming the monolayers, the bigger organic molecule A separating these monolayers, and $m = 1$ for the divalent Dion-Jacobson or $m = 2$ for the monovalent Ruddlesden-Popper configuration [1]. While in the bulk case A is limited by the tolerance factor to {Cs, formamidinium, methylammonium}, in the case of 2D perovskites A can be chosen from a plethora of organic molecules [1].

For this study Ruddlesden-Popper $m = 2$ thin films of PEA [phenethylammonium (C_6H_5) $\text{CH}_2\text{CH}_2\text{NH}_3$] lead iodide, $(\text{PEA})_2\text{PbI}_4$, were chosen. For the synthesis, (PEA)I and PbI_2 were dissolved in N,N-dimethylformamide in 2:1 molar ratio to obtain a solution of 8.3 wt.% concentration of $(\text{PEA})_2\text{PbI}_4$. The solution was spin-coated on glass substrates (the substrates had been washed by sonication at 60°C with detergent, water, acetone, isopropanol, and then UV-ozone treated) for 5 s at 400 rpm followed by 30 s at 3000 rpm. The obtained films were annealed on a hotplate at 100°C for 10 min. Spin-coating and annealing were carried out in a N_2 -filled glovebox. The procedure described here is an adaptation of that described in Ref. 2.

The lead(II) iodide (PbI_2 , 99%) and Phenethylamine ($\geq 99\%$) were purchased from Sigma-Aldrich. The hydriodic acid (57% aqueous solution, stabilized with 1.5% hypophosphorous acid) was purchased from ABCR. The N,N-Dimethylformamide (99.8%, Extra Dry over Molecular Sieve, AcroSeal) was purchased from Acros. All chemicals were used as received without further purification. The synthesis of phenethylammonium iodide ((PEA)I) was performed in-house and is described in the Supporting Information, S1.1.

Results of XRD, AFM, and profilometer characterization of the samples are given in Ref. [3]. The crystals consist of a stack of about 54 perovskite monolayers, separated from one another by a pair of PEA molecules. The perovskite monolayers are formed by PbI_4 corner shared octahedra. The length of the octahedra is $2 \times 3.17 \text{ \AA}$ [4], and the pair of PEA molecules separate those monolayers by 10.05 \AA at the closest iodine to iodine contact [5]. The unit cell of the layered perovskite structure is larger due to PEA twisting and an octahedral tilt. The a , b , c axis lengths reported in Ref. 2 are $a = b = 8.74 \text{ \AA}$, $c = 33.00 \text{ \AA}$ for the room temperature crystal configuration.

A. Synthesis of phenethylammonium iodide (PEA)I

As a special detail in the description of the sample growth, the synthesis of (PEA)I is presented. 13 ml of hydriodic acid was added dropwise to a mixture of 10 ml of phenethylamine and 20 ml of ethanol (anhydrous) while stirring. The mixture was cooled with an ice bath and stirred for 1 hour. The resulting solution was evaporated in a rotary evaporator at 50°C until the liquid was completely removed. The obtained solid was washed three times with diethylether and recrystallized from ethanol with diethylether. The final product of (PEA)I was obtained after drying under vacuum at 50°C overnight (14 g).

S2. EXPERIMENTAL RESULTS

A. Polarization of SFRS

In Figure S1(a), the SFRS spectra in circularly co-polarized and cross-polarized configuration at $\theta = 22^\circ$ for $B = 6 \text{ T}$ are shown. In the anti-Stokes and Stokes ranges, the electron spin-flip is clearly visible with a Raman shift of $|E_e| = 0.75 \text{ meV}$. Note that the absolute SFRS intensities of the electron spin-flip Raman peaks do not differ in the co- and cross-polarization configurations. The minor changes are originating from variations of the resonant photoluminescence background which is weaker in the σ^+/σ^+ configuration (blue spectrum).

In Figure S1(b) the SFRS spectra for the different linear co- and cross-polarizations are presented, measured in the Voigt geometry ($\theta = 90^\circ$) at $B_V = 7 \text{ T}$. The Raman shift of the electron spin-flip is

$|E_{e,(a,b)}| = 1.03 \text{ meV}$. With increasing tilt angle, the spin-flip process efficiency increases, so that the electron spin-flip intensity in the Stokes and anti-Stokes ranges increases approximately five times in comparison to $\theta = 22^\circ$. The comparison of the different linear polarization configurations shows that the absolute electron SFRS peak intensity is only 20% weaker in the cross-linear configurations than in the co-linear configurations, both for Stokes and anti-Stokes.

B. SFRS temperature dependence

Experimental data on the temperature dependence of SFRS measured in the Voigt geometry are given in Figure S2. The SFRS anti-Stokes spectra at temperatures of 5 K and 12 K are presented in Figure S2a. At $T = 5 \text{ K}$

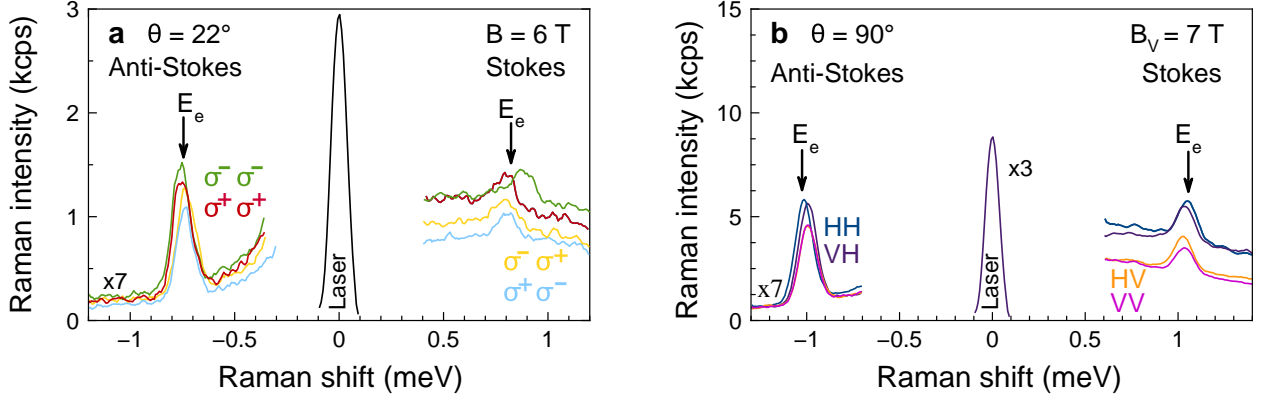


FIG. S1. SFRS spectra measured in the anti-Stokes and the Stokes ranges for $E_{\text{exc}} = 2.345$ eV photon energy using a power $P = 5.7$ W/cm² at $T = 1.6$ K. (a) SFRS in tilted field geometry with $\theta = 22^\circ$ for both co- and cross-circular polarization at $B = 6$ T. (b) SFRS in Voigt geometry for co- and cross-linear polarization at $B_V = 7$ T. The linear polarizations H and V are given for excitation / detection. The anti-Stokes spectra are multiplied with a factor of 7 to increase the visibility of the SFRS lines. The electron E_e and the combined E_{e+h} spin-flip Raman peak positions are marked by arrows.

the electron (E_e) and double (E_{e+h}) spin-flip lines are pronounced compared to 12 K, where only the weak electron spin-flip remains visible. The Raman shift is not affected by temperature as shown by the temperature dependence of the electron g -factor in Figure S2c: the electron g -factor remains constant, $g_{e,(a,b)} = 2.5 \pm 0.1$, in the temperature range from 1.6 K up to 16 K, as one would expect from the negligible changes of the band structure in this range.

The amplitude of the electron spin-flip line decreases with increasing temperature, but is hardly detectable above 16 K. The temperature dependence of the SFRS intensity is shown by the green circles in Figure S2b and

can be described by the Arrhenius-like equation

$$I(T) = \left(A \exp\left(\frac{E_A}{k_B T}\right) + C \right)^{-1}, \quad (\text{S1})$$

with the activation energy E_A and the Boltzmann constant k_B .

From fitting the data, the parameters amount to $E_A = 2.1$ meV, with the amplitude $A = 0.22$ and the constant $C = 0.0075$ (see the line in Figure S2b). We suggest that the thermal delocalization of resident electrons is the mechanism that leads to the reduction of the efficiency of the SFRS process. Moreover, in Figure S2b the temperature dependence of the full width at half maximum (FWHM) of the electron spin-flip line is presented which has a rather constant value of about 0.1 meV within the examined temperature range.

-
- [1] L. Mao, C. C. Stoumpos, M. G. Kanatzidis, Two-dimensional hybrid halide perovskites: principles and promises. *J. Am. Chem. Soc.* **2018**, *141*, 1171.
- [2] K.-z. Du, Q. Tu, X. Zhang, Q. Han, J. Liu, S. Zauscher, D. B. Mitzi, Two-dimensional lead (II) halide-based hybrid perovskites templated by acene alkylamines: crystal structures, optical properties, and piezoelectricity. *Inorg. Chem.* **2017**, *56*, 9291.
- [3] E. Kirstein, E. A. Zhukov, D. R. Yakovlev, N. E. Kopteva, C. Harkort, D. Kudlacik, O. Hordiichuk, M. V. Kovalenko, M. Bayer, Coherent spin dynamics of electrons in two-dimensional (PEA)₂PbI₄ perovskites. *Nano Letters* **2023**, *23*, 205.
- [4] J. Hu, I. W. H. Oswald, S. J. Stuard, M. M. Nahid, N. Zhou, O. F. Williams, Z. Guo, L. Yan, H. Hu, Z. Chen, X. Xiao, Y. Lin, Z. Yang, J. Huang, A. M. Moran, H. Ade, J. R. Neilson, W. You, Synthetic control over orientational degeneracy of spacer cations enhances solar cell efficiency in two-dimensional perovskites. *Nature Commun.* **2019**, *10*, 1276.
- [5] E. Mahal, S. Charan Mandal, B. Pathak, Understanding the role of spacer cation in 2D layered halide perovskites to achieve stable perovskite solar cells. *Mater. Adv.* **2022**, *3*, 2464.

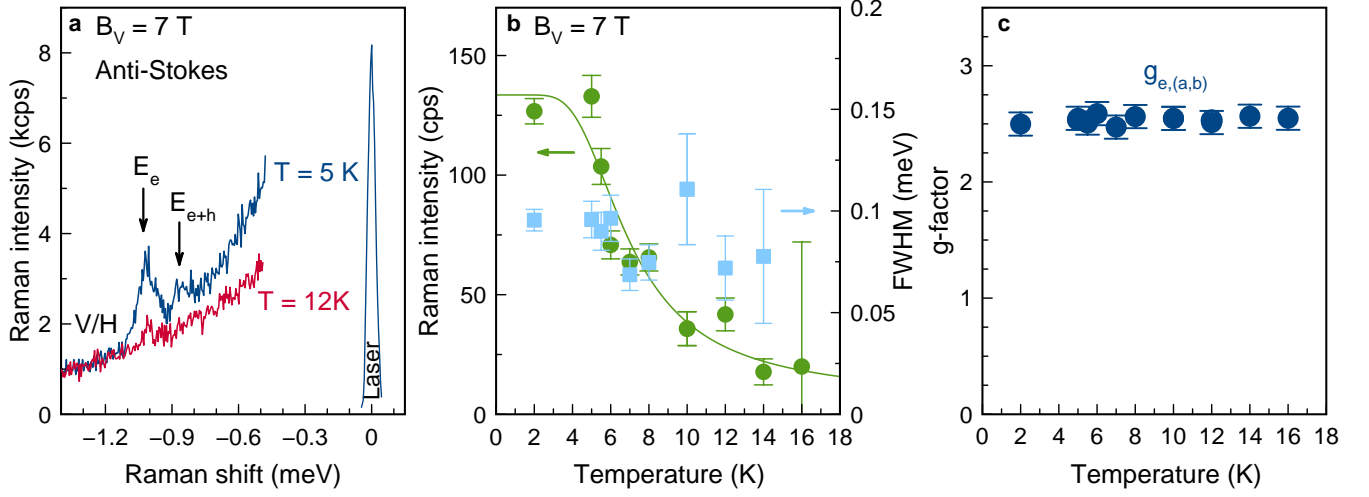


FIG. S2. Temperature dependence of SFRS in $(\text{PEA})_2\text{PbI}_4$ measured in the Voigt geometry. (a) Anti-Stokes SFRS spectra at $T = 5$ K (blue) and 12 K (red), measured at $B_V = 7$ T. Both spectra are multiplied by a factor of 10 in order to increase the visibility of the spin-flip signals. (b) Temperature dependence of the electron SFRS intensity (green circles) and the full width at half maximum (blue squares). The temperature behavior of the electron intensity follows the Arrhenius-like equation (S1) shown by the green line fit. (c) Temperature dependence of the electron g -factor.